NUMERICAL INVESTIGATION OF HYPERSONIC TURBULENT BOUNDARY LAYERS WITH HIGH-TEMPERATURE EFFECTS

D. Passiatore[1], L. Sciacovelli[2], P. Cinnella[3] & G. Pascazio[1]

[1]Politecnico di Bari, DMMM, via Re David 200, 70125 Bari, Italy.
[2]Arts et Métiers Institute of Technology, DynFluid Laboratory, 151 bd. de l'Hôpital, 75013 Paris, France.
[3]Sorbonne Université, Institut Jean Le Rond d'Alembert, 4 Place Jussieu, 75005 Paris, France.

Abstract

A hypersonic turbulent boundary layer over a flat plate is numerically investigated. The large Mach number and temperature values in the freestream ($M_e = 12.48$ and $T_e = 594.3\,\mathrm{K}$, respectively) lead to a high-enthalpy regime and to the occurrence of thermochemical non-equilibrium effects. Vibrational relaxation phenomena are shown to be predominant with respect to chemical activity. In this context, high-fidelity results obtained by means of a Direct Numerical Simulation (DNS) are used as a benchmark to assess the quality of a Large-Eddy Simulation (LES) performed with a coarser wall-resolved grid. The wall-adapting local eddy viscosity approach is selected as sub-grid scale (SGS) model. The LES strategy is shown to capture the mean and fluctuating dynamic fields in the fully turbulent region quite satisfactorily, whereas transition to turbulence is slightly anticipated with respect to DNS. Both the chemical and vibrational source terms are evaluated with the filtered aerothermochemical quantities, resulting in an overestimation of the translational-vibrational energy exchange and an underestimation of dissociation chemical production rates. These results shed light on the necessity of developing more accurate closure models for the source terms, the SGS turbulence-thermochemistry interactions being important for the configuration under investigation.

Keywords: hypersonic boundary-layers, turbulence, high-fidelity simulations, LES, thermochemical non-equilibrium

1. Introduction

High-speed flows are encountered in a wide range of applications, including reentry vehicles, spatial tourism or trans-atmospheric flights. An accurate knowledge of the flow surrounding such flying vehicle is crucial to accurately design the Thermal Protection System (TPS) and to prevent excessive aerodynamic heating. The high temperatures reached in these regimes can cause vibrational excitation of the gas molecules and chemical reactions (both with characteristic times similar to those of the fluid motion), giving rise to a thermochemical nonequilibrium state. At the same time, the flow may be subjected to a transition from a laminar to a turbulent regime, due to TPS erosion or freestream disturbances, especially in low-altitude flights (i.e., higher Reynolds numbers). Transition to turbulence and compressible turbulence at high-enthalpy conditions are two physical phenomena not well understood yet; the coupling between high-temperature effects and turbulent flows is an even more unexplored research area which has raised particular interest in the scientific community.

Most advanced studies in this area rely on Computational Fluid Dynamics (CFD) analyses, since carrying out physical experiments in such working conditions is often a difficult and expensive task. In this context, high-fidelity numerical simulations provide a powerful tool, giving access to all active spatial and temporal scales and avoiding the introduction of modelling errors. Nevertheless, one has to deal with the computational cost of performing Direct Numerical Simulations (DNS); the already excessive computational cost of solving the direct problem is further increased by the need of solving additional conservation equations for multi-component flows. The immediate consequence is that

such computations are usually limited to simple geometries and relatively small Reynolds numbers; the challenging DNS recently performed for high-enthalpy flows are standalone computations, since parametric studies are yet unfeasible with the computational power currently available. The numerical prediction of aerodynamic forces and heating in practical flight configurations still largely relies on the solution of the Favre-averaged Navier–Stokes equations (FANS), which requires the use of appropriate turbulence models to represent the unclosed terms in the governing equations. Unfortunately, such a methodology introduces several inaccuracies: the existing closure models, mainly developed for incompressible flows and then extended to compressible configurations, offer only a rough approximation for modeling turbulence dynamics. Another option, which still requires a significant computational effort with respect to FANS, consists in the use of Large-Eddy Simulations (LES), which relax the spatial discretization constraints of the DNS by adding a model for the unresolved subgrid scales (SGS). In this context, however, the selection of a suitable numerical strategy plays an important role. A compromise between the needs of accurate representation of the range of temporal and spatial scales and numerical stabilization has to be found when considering under-resolved configurations. The computational cost of a LES can be further decreased by making use of a wall model formulation (WMLES). Nevertheless, the choice of a suitable wall model taking into account thermochemical non-equilibrium effects is not currently available and requires relevant scientific efforts. For this reason, the present work focuses on a wall-resolved LES, for which no wall-model is needed since the near-wall physics is captured by the selected computational grid.

In the past years, a series of LES of supersonic turbulent boundary-layer flows have been performed [1, 2, 3, 4, 5] and more recently hypersonic flows configurations have gained particular attention [6, 7]. Globally, mean turbulent quantities are well reproduced by a highly-resolved LES, whereas it is a common agreement that transition processes, flow separation, peak of wall heat transfer and skin friction hardly collapse with the high-fidelity benchmark data, mainly because of the numerical errors introduced. To the authors' knowledge, LESs of high-enthalpy turbulent flows have never been performed so far, whereas a big contribution in terms of DNS databases has been recently given by [8], [9] and [10]. In [11], a formulation for a WMLES of hypersonic and high enthalpy flows is proposed, highlighting the necessity of performing analyses of LES results to corroborate the a priori statements; thus, the present work can be viewed as a starting point for the comprehension of LES modeling of high-enthalpy flows.

The configuration under investigation is a hypersonic compressible turbulent boundary-layer, chemically and thermally out-of-equilibrium, in the same conditions of [10]. The statistical field of the DNS performed in [10] will be used as a benchmark to assess the accuracy of the results obtained by means of a LES, based on the Wall-Adapting Local Eddy-viscosity (WALE) [12]. The aim of the present work is then to assess the capability of the numerical strategy to accurately predict compressible flows chemically and thermally out-of-equilibrium and to prove the suitability of the scheme in faithfully representing the turbulence dynamics.

The paper is structured as follows. Subsection 2.1 reports the governing equations, along with the LES model adopted, and the models used for thermodynamics, thermochemistry and transport properties. In subsection 2.2 and 2.3 the numerical strategy and the problem setup are presented. The discussion of the results and the conclusions of the present work are then illustrated in sections 3. and 4.

2. Methodology

2.1 Governing equations

In this work, the fluid under investigation is high-temperature air, modeled as a five-species mixture of N_2, O_2, NO, O and N. The behavior of such high-enthalpy flows is governed by the compressible Navier–Stokes equations for multicomponent, chemically-reacting and thermally-relaxing gases [13]. Differently from DNS, where the Navier–Stokes equations are directly integrated, the LES approach consists in solving the filtered equations. Denoting with $\overline{f}$ the classical filter and with $\widetilde{f} \equiv \frac{\overline{\rho f}}{\overline{\rho}}$ the

mass-weighted Favre filtering, the resulting filtered system reads

$$\frac{\partial \overline{\rho}}{\partial t} + \frac{\partial \overline{\rho}\widetilde{u}_j}{\partial x_j} = 0 \tag{1}$$

$$\frac{\partial \overline{\rho}\widetilde{u}_i}{\partial t} + \frac{\partial \left(\overline{\rho}\widetilde{u}_i\widetilde{u}_j + \overline{p}\delta_{ij}\right)}{\partial x_j} = \frac{\partial \overline{\tau}_{ij}}{\partial x_j} - \frac{\partial}{\partial x_j}\left[\overline{\rho}\left(\widetilde{u_i u_j} - \widetilde{u}_i\widetilde{u}_j\right)\right] \tag{2}$$

$$\frac{\partial \overline{\rho}\widetilde{E}}{\partial t} + \frac{\partial \left[\left(\overline{\rho}\widetilde{E} + \overline{p}\right)\widetilde{u}_j\right]}{\partial x_j} = \frac{\partial \left(\widetilde{u}_i\overline{\tau}_{ij}\right)}{\partial x_j} - \frac{\partial}{\partial x_j}\left(-\widetilde{\lambda}_{\mathsf{TR}}\frac{\partial \widetilde{T}}{\partial x_j} + -\widetilde{\lambda}_{\mathsf{V}}\frac{\partial \widetilde{T_V}}{\partial x_j}\right) - \frac{\partial}{\partial x_j}\left(\sum_{n=1}^{\mathsf{NS}}\overline{\rho}_n\widetilde{u}_{nj}^D\widetilde{h}_n\right) \tag{3}$$

$$- \frac{\partial}{\partial x_j}\left(\widetilde{u_i\tau_{ij}} - \widetilde{u}_i\overline{\tau}_{ij}\right) - \frac{\partial}{\partial x_j}\left[\overline{\rho}\left(\widetilde{hu_j} - \widetilde{h}\widetilde{u}_j\right)\right]$$

$$\frac{\partial \overline{\rho}\widetilde{Y}_n}{\partial t} + \frac{\partial \left(\overline{\rho}\widetilde{Y}_n\widetilde{u}_j\right)}{\partial x_j} = -\frac{\partial \overline{\rho}_n\widetilde{u}_{nj}^D}{\partial x_j} + \overline{\dot{\omega}}_n - \frac{\partial}{\partial x_j}\left[\overline{\rho}\left(\widetilde{Y_n u_j} - \widetilde{Y}_n\widetilde{u}_j\right)\right] \qquad (n = 1, .., \mathsf{NS} - 1) \tag{4}$$

$$\frac{\partial \overline{\rho}\widetilde{e}_{\mathsf{V}}}{\partial t} + \frac{\partial \overline{\rho}\widetilde{e}_{\mathsf{V}}\widetilde{u}_j}{\partial x_j} = \frac{\partial}{\partial x_j}\left(-\widetilde{\lambda}_{\mathsf{V}}\frac{\partial \widetilde{T_V}}{\partial x_j} - \sum_{m=1}^{\mathsf{NM}}\overline{\rho}_m\widetilde{u}_{mj}^D\widetilde{e}_{\mathsf{V}m}\right) + \overline{\sum_{m=1}^{\mathsf{NM}}\left(Q_{\mathsf{TV}m} + \dot{\omega}_m e_{\mathsf{V}m}\right)} \tag{5}$$

$$- \frac{\partial}{\partial x_j}\left[\overline{\rho}\left(\widetilde{u_j e_{\mathsf{V}}} - \widetilde{u}_j\widetilde{e}_{\mathsf{V}}\right)\right].$$

In the preceding system, $\overline{\rho}$ is the filtered mixture density, t the time coordinate, x_j the space coordinate in the j-th direction of a Cartesian system, with $\widetilde{u}_j$ the filtered velocity vector component in the same directions; $\overline{p}$ is the filtered pressure and $\overline{\tau}_{ij}$ the viscous stress tensor based on the gradients of the filtered velocities, modeled as

$$\overline{\tau}_{ij} = \widetilde{\mu}\left(\frac{\partial \widetilde{u}_i}{\partial x_j} + \frac{\partial \widetilde{u}_j}{\partial x_i}\right) - \frac{2}{3}\widetilde{\mu}\frac{\partial \widetilde{u}_k}{\partial x_k}\delta_{ij}, \tag{6}$$

with $\widetilde{\mu}$ the filtered mixture dynamic viscosity and δ_{ij} the Kronecker symbol. The conservation of total filtered energy $\widetilde{E} = \widetilde{e} + \frac{1}{2}\widetilde{u}_i\widetilde{u}_i$ is expressed by means of equation (3), where $\widetilde{e}$ is the filtered mixture internal energy, $-\widetilde{\lambda}_{\mathsf{TR}}\frac{\partial \widetilde{T}}{\partial x_j}$ and $-\widetilde{\lambda}_{\mathsf{V}}\frac{\partial \widetilde{T_V}}{\partial x_j}$ are the roto-translational and vibrational contributions to the heat flux, $\widetilde{\lambda}_{\mathsf{TR}}$ and $\widetilde{\lambda}_{\mathsf{V}}$ being the filtered roto-translational and vibrational thermal conductivities, respectively. In order to take into account thermal non-equilibrium, two different temperatures are used, $\widetilde{T}$ being the filtered roto-translational temperature (called hereafter only "translational" for the sake of simplicity) and $\widetilde{T}_V$ the filtered vibrational one. $\widetilde{u}_{nj}^D$ denotes the filtered diffusion velocity and $\widetilde{h}_n$ the filtered specific enthalpy for the n-th species. In the species conservation equations (4), $\overline{\rho}_n = \overline{\rho}\widetilde{Y}_n$ represents the n-th species filtered partial density ($\widetilde{Y}_n$ being the filtered mass fraction) and $\overline{\dot{\omega}}_n$ the filtered rate of production of the n-th species. To ensure total mass conservation, the mixture density and NS -1 species conservation equations are solved, while the density of the NS-th species is computed as $\overline{\rho}_{\mathsf{NS}} = \overline{\rho} - \sum_{n=1}^{\mathsf{NS}-1}\overline{\rho}_n$. In the following, we set such species as molecular nitrogen, since it is the most abundant one throughout the computational domain. As for equation (5), $\widetilde{e}_{\mathsf{V}} = \sum_{m=1}^{\mathsf{NM}}\widetilde{Y}_m\widetilde{e}_{\mathsf{V}m}$ represents the filtered mixture vibrational energy, with $\widetilde{e}_{\mathsf{V}m}$ the filtered vibrational energy of the m-th molecule and NM their total number. Only one additional equation for the conservation of mixture vibrational energy is employed, relying on the assumption that the vibrational energetic modes of the three molecular species in the mixture are equilibrated with each other at the same $\widetilde{T}_V$. In the same equation, $\overline{Q_{\mathsf{TV}}} = \sum_{m=1}^{\mathsf{NM}}\overline{Q_{\mathsf{TV}m}}$ represents the energy exchange between vibrational and translational modes due to molecular collisions and $\sum_{m=1}^{\mathsf{NM}}\overline{\dot{\omega}_m e_{\mathsf{V}m}}$ the vibrational energy lost or gained due to molecular depletion or production, both computed with the filtered variables. Each species is assumed to behave as a thermally-perfect gas; Dalton's pressure mixing law leads then to the thermal equation of state:

$$\overline{p} = \overline{\rho}\widetilde{T}\sum_{n=1}^{\mathsf{NS}}\frac{\mathscr{R}\widetilde{Y}_n}{\mathscr{M}_n} = \widetilde{T}\sum_{n=1}^{\mathsf{NS}}\overline{\rho}_n R_n, \tag{7}$$

R_n and $\mathscr{M}_n$ being the gas constant and molecular weight of the n-th species, respectively, and $\mathscr{R} = 8.314$ J/mol K the universal gas constant. The thermodynamic properties of high-temperature air

species are computed considering the contributions of translational, rotational and vibrational (TRV) modes:

$$\widetilde{e} = \sum_{n=1}^{NS} \widetilde{Y}_n \widetilde{h}_n - \frac{\overline{p}}{\overline{\rho}} = \widetilde{h} - \frac{\overline{p}}{\overline{\rho}}, \quad \text{with} \quad \widetilde{h}_n = h_{f,n}^0 + \widetilde{h}_n^{TR} + \widetilde{e}_{Vn}. \tag{8}$$

Here, $h_{f,n}^0$ is the n-th species enthalpy of formation at the reference temperature ($T_{ref} = 298.15\,\text{K}$), $\widetilde{h}_n^{TR}$ is the roto-translational specific enthalpy and $\widetilde{e}_{Vn}$ the vibrational energy of species n. These terms read:
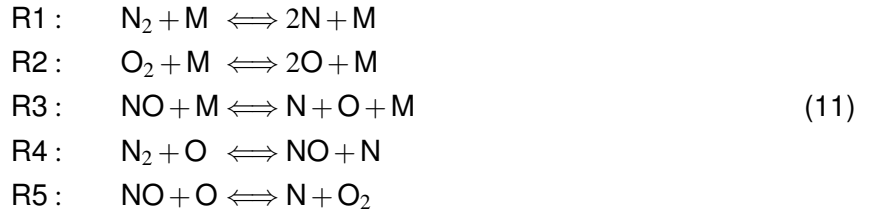
$$\widetilde{h}_n^{TR} = \int_{T_{ref}}^{\widetilde{T}} (c_{p,n}^T + c_{p,n}^R)\, d\widetilde{T}' \quad \text{with} \quad c_{p,n}^T = \frac{5}{2}R_n, \quad c_{p,n}^R = \begin{cases} R_n & \text{for diatomic species} \\ 0 & \text{for monoatomic species} \end{cases} \tag{9}$$

and

$$\widetilde{e}_{Vn} = \begin{cases} \dfrac{\theta_n R_n}{\exp(\theta_n/\widetilde{T}_V) - 1} & \text{for diatomic species} \\ 0 & \text{for monoatomic species} \end{cases} \tag{10}$$

θ_n being the characteristic vibrational temperature of each molecule ($3393\,\text{K}$, $2273\,\text{K}$ and $2739\,\text{K}$ for N_2, O_2 and NO, respectively). After the numerical integration of the conservation equations, the roto-translational temperature $\widetilde{T}$ is computed from the specific internal energy (devoid of the vibrational contribution) directly, whereas an iterative Newton–Raphson method is used to compute $\widetilde{T}_V$ from $\widetilde{e}_V = \sum_{m=1}^{NM} \widetilde{Y}_m \widetilde{e}_{Vm}$.

To close the system, we use Park's two-temperatures (2T) model [14] to take into account the contextual presence of thermal and chemical non-equilibrium for the computation of $\overline{\dot{\omega}}_n$ and $\overline{Q_{TV}}$. Specifically, the five species interact with each other through a reaction mechanism consisting of five reversible chemical steps [15]:

$$\begin{array}{lll} \text{R1:} & N_2 + M & \Longleftrightarrow 2N + M \\ \text{R2:} & O_2 + M & \Longleftrightarrow 2O + M \\ \text{R3:} & NO + M & \Longleftrightarrow N + O + M \\ \text{R4:} & N_2 + O & \Longleftrightarrow NO + N \\ \text{R5:} & NO + O & \Longleftrightarrow N + O_2 \end{array} \tag{11}$$

M being the third body (any of the five species considered). Dissociation and recombination processes are described by reactions R1, R2 and R3, whereas the shuffle reactions R4 and R5 represent rearrangement processes. The mass rate of production of the n-th species is governed by the law of mass action:

$$\overline{\dot{\omega}}_n = \mathscr{M}_n \sum_{r=1}^{NR} \left(v_{nr}'' - v_{nr}'\right) \times \left[\overline{k_{f,r}} \prod_{n=1}^{NS} \left(\frac{\overline{\rho} \widetilde{Y}_n}{\mathscr{M}_n}\right)^{v_{nr}'} - \overline{k_{b,r}} \prod_{n=1}^{NS} \left(\frac{\overline{\rho} \widetilde{Y}_n}{\mathscr{M}_n}\right)^{v_{nr}''}\right], \tag{12}$$

where v_{nr}' and v_{nr}'' are the stoichiometric coefficients for reactants and products in the r-th reaction for the n-th species, respectively, and NR is the total number of reactions. Furthermore, $\overline{k_{f,r}}$ and $\overline{k_{b,r}}$ denote the forward and backward r-th reaction rates, modeled by means of Arrhenius' law and computed with the filtered quantities. The coupling between chemical and thermal nonequilibrium is taken into account by means of a modification of the temperature values used for computing the reaction rates. Indeed, a geometric-averaged temperature is considered for the dissociation reactions R1, R2 and R3 in (11), computed as $T_{avg} = \widetilde{T}^q \widetilde{T}_V^{1-q}$ with $q = 0.7$ [14]. Lastly, the vibrational-translational energy exchange is computed as:

$$\overline{Q_{TV}} = \sum_{m=1}^{NM} \overline{Q_{TV,m}} = \sum_{m=1}^{NM} \overline{\rho}_m \frac{\widetilde{e}_{Vm}(\widetilde{T}) - \widetilde{e}_{Vm}(\widetilde{T}_V)}{\overline{\tau}_m}, \tag{13}$$

where $\overline{\tau}_m$ is the molecule relaxation time evaluated by means of the expression of Millikan & White [16]. The mean value is then evaluated with a weighted harmonic average:

$$\overline{\tau}_m = \sum_{n=1}^{NS} \frac{\overline{\rho}_n}{\mathscr{M}_n} \sum_{n=1}^{NS} \frac{\overline{\tau}_{mn}^{MW}}{\overline{\rho}_n / \mathscr{M}_n} \tag{14}$$

and the relaxation time of the m-th molecule with respect to the n-th species writes

$$\overline{\tau}_{mn}^{\text{MW}} = \frac{\overline{p}}{p_{\text{atm}}} \exp\left[a_{mn}(\widetilde{T}^{-\frac{1}{3}} - b_{mn}) - 18.42\right],\tag{15}$$

where $p_{\text{atm}} = 101325\,\text{Pa}$ and a_{mn} and b_{mn} are coefficients reported in [17]. As for the computation of the transport properties, pure species' viscosity and thermal conductivities are computed using Blottner's curve-fits [18] and Eucken's relations [19], respectively. The corresponding mixture properties are evaluated by means of Wilke's mixing rules [20]. Mass diffusion is modeled by means of Fick's law:

$$\overline{\rho}_n \widetilde{u}_{nj}^D = -\overline{\rho}\overline{D}_n \frac{\partial \widetilde{Y}_n}{\partial x_j} + \overline{\rho}_n \sum_{n=1}^{\text{NS}} \overline{D}_n \frac{\partial \widetilde{Y}_n}{\partial x_j},\tag{16}$$

where the first term on the r.h.s. represents the effective diffusion velocity and the second one is a mass corrector term that should be taken into account in order to satisfy the continuity equation when dealing with non-constant species diffusion coefficients [21]. Specifically, $\overline{D}_n$ is a filtered equivalent diffusion coefficient of species n into the mixture, computed following Hirschfelder's approximation [19], starting from the binary diffusion coefficients which are curve-fitted in [22]. Further details about the selected models and the underlying hypotheses can be found in Passiatore *et al.* [10].

In equations (2)-(5), the subgrid-scale fluxes that have to be modeled are:

$$\overline{\rho}\left(\widetilde{u_i u_j} - \widetilde{u}_i \widetilde{u}_j\right)\tag{17}$$

$$\overline{\rho}\left(\widetilde{h u_j} - \widetilde{h}\widetilde{u}_j\right)\tag{18}$$

$$\overline{\rho}\left(\widetilde{Y_n u_j} - \widetilde{Y}_n \widetilde{u}_j\right)\tag{19}$$

$$\overline{\rho}\left(\widetilde{u_j e_V} - \widetilde{u}_j \widetilde{e}_V\right)\tag{20}$$

which correspond to the SGS stress tensor (τ_{ij}^{SGS}), and to the SGS enthalpy, species and vibrational energy fluxes, respectively. The first is modeled by means of the definition of a SGS eddy viscosity μ_{SGS}, given by

$$\overline{\rho}\left(\widetilde{u_i u_j} - \widetilde{u}_i \widetilde{u}_j\right) = \tau_{ij}^{\text{SGS}} - \frac{1}{3}\tau_{kk}^{\text{SGS}} = -2\mu_{\text{SGS}}\left(\widetilde{S}_{ij} - \frac{1}{3}\widetilde{S}_{kk}\delta_{ij}\right),\tag{21}$$

where $\widetilde{S}_{ij} = \frac{1}{2}\left(\frac{\partial \widetilde{u}_i}{\partial x_j} + \frac{\partial \widetilde{u}_j}{\partial x_i}\right)$ denotes the strain-rate tensor of the resolved scales. The SGS eddy viscosity is then computed using the invariant of the velocity gradient tensor, based on the Wall-Adapting Local Eddy-viscosity (WALE) [12] model. Specifically, one has

$$\mu_{\text{SGS}} = \overline{\rho}C_w^2\Delta^2 \frac{(\widetilde{S}_{ij}^* \widetilde{S}_{ij}^*)^{3/2}}{(\widetilde{S}_{ij}\widetilde{S}_{ij})^{5/2} + (\widetilde{S}_{ij}^* \widetilde{S}_{ij}^*)^{5/4}},\tag{22}$$

with

$$\widetilde{S}_{ij}^* = \frac{1}{2}\left(\widetilde{g}_{ik}\widetilde{g}_{kj} + \widetilde{g}_{jk}\widetilde{g}_{ki}\right) - \frac{1}{3}\widetilde{g}_{kk}^2 \delta ij\tag{23}$$

Here, C_w is a modeling constant set equal to 0.325, $\Delta = (\Delta x \Delta y \Delta z)^{1/3}$ is a measure of the local grid size and $\widetilde{g}_{ij}$ represents to the resolved velocity gradient $\partial \widetilde{u}_i/\partial x_j$. Of note, the isotropic part of the SGS stress tensor τ_{kk}^{SGS} is not modeled. The remaining SGS fluxes (18)-(20) are modeled using a simple gradient-diffusion hypothesis; for the SGS enthalpy and vibrational energy fluxes, the approximation writes

$$\overline{\rho}\left(\widetilde{h u_j} - \widetilde{h}\widetilde{u}_j\right) = -\frac{\mu_{\text{SGS}}}{Pr_{\text{SGS}}}\frac{\partial \widetilde{(h - e_V)}}{\partial x_j} - \frac{\mu_{\text{SGS}}}{Pr_{V,\text{SGS}}}\frac{\partial \widetilde{e}_V}{\partial x_j}\tag{24}$$

$$\overline{\rho}\left(\widetilde{u_j e_V} - \widetilde{u}_j \widetilde{e}_V\right) = -\frac{\mu_{\text{SGS}}}{Pr_{V,\text{SGS}}}\frac{\partial \widetilde{e}_V}{\partial x_j},\tag{25}$$

Pr_{SGS} and $Pr_{V,SGS}$ being the turbulent Prandtl number and turbulent vibrational Prandtl number, respectively. If $Pr_{SGS} = Pr_{V,SGS}$ there is no need to separate the two contributions in equation (24). In a similar way, the SGS mass flux can be modeled as

$$\overline{\rho} \left(\widetilde{Y_n u_j} - \widetilde{Y}_n \widetilde{u}_j \right) = - \frac{\mu_{SGS}}{Sc_{n,SGS}} \frac{\partial \widetilde{Y}_n}{\partial x_j}, \tag{26}$$

$Sc_{n,SGS}$ being the eddy Schmidt number of species n. The remaining unclosed term in the total energy equation (3) is then computed as

$$\widetilde{u_i \tau_{ij}} - \widetilde{u}_i \overline{\tau}_{ij} = \tau_{ij}^{SGS} \frac{\partial \widetilde{u}_i}{\partial x_j}. \tag{27}$$

In our simulation, we set $Pr_{SGS} = 0.9$, $Pr_{V,SGS} = 0.9$ and $Sc_{n,SGS} = 1.0$, based also on a priori considerations in [8, 9, 10].

2.2 Numerical method

The numerical scheme employed for spatial discretization is the same for both DNS and LES computations. Specifically, the two sets of governing equations are integrated by using a high-order centered finite-difference scheme. The convective fluxes are discretized by means of central tenth-order differences, supplemented with an adaptive artificial dissipation. The latter consists in a blend of a ninth-order-accurate dissipation term based on tenth-order derivatives of the conservative variables (used to damp grid-to-grid oscillations) along with a low-order shock-capturing term. A highly-selective sensor, based on Ducros' extension of Jameson's pressure-based sensor [23] is used to turn on shock capturing in the immediate vicinity of flow discontinuities. For the vibrational energy equation (5), a shock sensor based on second-order derivatives of the vibrational temperature was preferred to ensure appropriate damping of spurious oscillations. Finally, time integration is carried out by means of a third-order TVD Runge-Kutta scheme [24]. Further details on the numerical strategy can be found in Sciacovelli *et al.* [25].

2.3 Problem setup

The configuration under investigation is a spatially-evolving, flat-plate boundary layer with cooled walls. To avoid confusion between DNS and LES, we will now omit the filter operator; the reader would know that when we refer to LES results, we are considering filtered quantities. The prescribed edge conditions of $M_e = 12.48$, $T_e = 594.3\,\mathrm{K}$ and $p_e = 4656\,\mathrm{Pa}$ are representative of those downstream of a shock wave generated by a $6°$ sharp wedge flying at $M = 20$ at an altitude of approximately $36\,\mathrm{km}$, recently investigated in [10]. Air at such free-stream conditions is in thermochemical equilibrium with $X_{N_2} = 0.79$, $X_{O_2} = 0.21$, X_n being the n-th species molar fraction. The calculation is initiated in the laminar region at a distance x_0 from the plate leading edge. As inlet boundary conditions, we imposed the profiles generated by solving the locally self-similar theory for a two-dimensional chemically out-of-equilibrium and vibrationally equilibrated boundary layer [25]; the inflow Reynolds number based on the inlet displacement thickness is $\mathrm{Re}_{\delta_{in}^\star} = 6000$. At the right and top boundary, characteristic-based boundary conditions are prescribed. The wall is assumed non-catalytic (*i.e.*, $\partial Y_\bullet / \partial y = 0$) and isothermal with $T = T_V = 1800\,\mathrm{K}$. Transition to turbulence is induced by means of a suction and blowing strategy, similar to the one adopted in [10]. The extent of the domain is $L_x \times L_y \times L_z = 3000\delta_{in}^\star \times 120\delta_{in}^\star \times 30\pi\delta_{in}^\star$. The computational grid for the DNS is $N_x \times N_y \times N_z = 9660 \times 480 \times 512$, whereas the LES simulation is performed halving the points in x- and z-direction ($4832 \times 480 \times 256$).

3. Results

In this section, the results of the LES computation are systematically compared to the reference DNS solution of [10], to assess the capabilities of the WALE model in reproducing the reference benchmark. To begin, figure 1 shows an instantaneous visualization of a xz-plane extracted at $y/\delta_{in}^* \approx 0.5$. The footprint of the suction and blowing forcing is clearly visible right after the inlet boundary condition. At approximately one third of the domain, the injected streaky structures start to destabilize and interact with the secondary (oblique) modes, inducing a sharp transitional region, before bursting in turbulence. We can observe that globally the dimensions and distribution of the turbulent structures
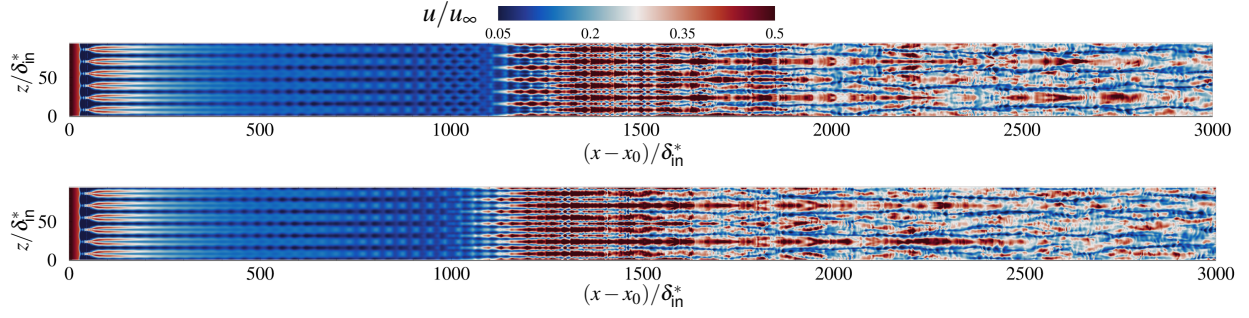
Figure 1 – Instantaneous visualizations of the normalized streamwise velocity in a *xz* plane for DNS (top) and LES (bottom) extracted at $y/\delta_{in}^* \approx 0.5$. The spanwise direction is stretched for better visualization.
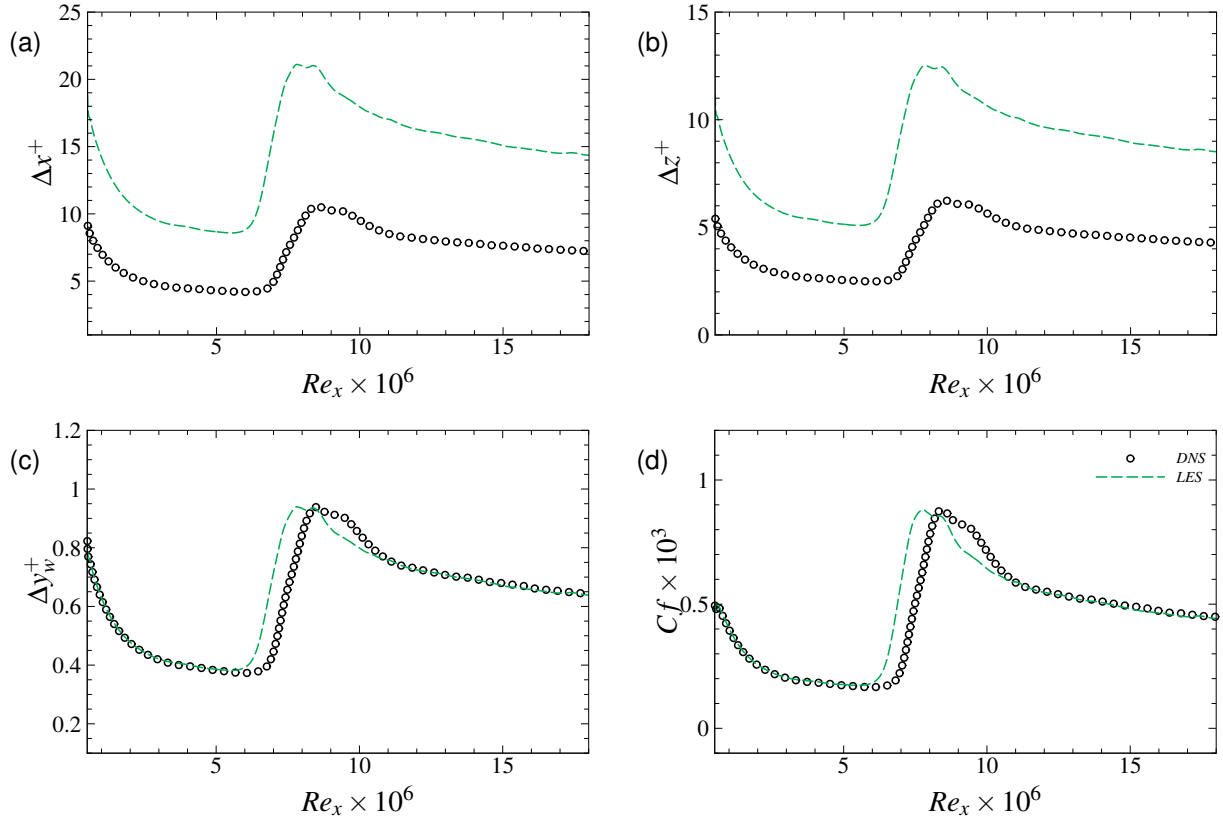

Figure 2 – Streamwise evolution of grid resolutions in wall units in the streamwise (a), spanwise (b) and wall-normal direction (c) and streamwise evolution of the skin friction coefficient (d).

is particularly similar in the region comprised between $(x-x_0)/\delta_{in}^* \approx 2000$ and $(x-x_0)/\delta_{in}^* \approx 3000$. The transitional region qualitatively presents the same trend, even if the formation of the fast structures that will induce the breakdown is anticipated in LES, as we will corroborate hereafter.

Figure 2(a)-(c) reports the streamwise evolution of Δx^+, Δz^+ and Δy_w^+ for the two simulations. The stricter resolution requirements are reached when the flow transitions to turbulence; in this region, the LES grid results in $\Delta x^+ \approx 20$ and $\Delta z^+ \approx 12$. In terms of Δy_w^+, the values stays under the unity throughout the entire computational domain (the grid point distribution in the y-direction being unaltered between the simulations). Nevertheless, a discrepancy with respect to the reference solution is observed at the transition, as also underlined in figure 2(d) by the evolution of the skin friction coefficient

$$C_f = \frac{\tau_w}{0.5\rho_\infty u_\infty^2} \quad (28)$$

where $\tau_w = \mu_w(\partial u/\partial y)|_w$ represents the wall shear stress. The profiles in the laminar region, in good
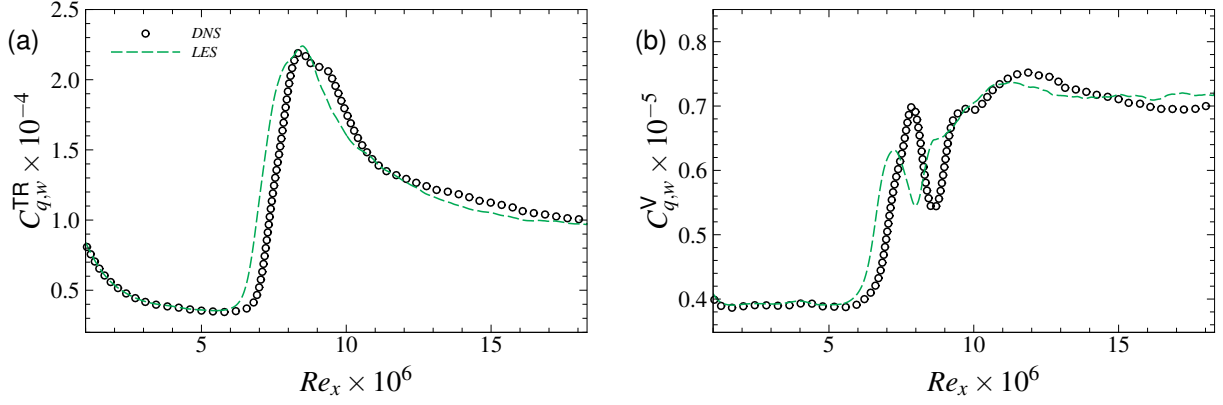
Figure 3 – Streamwise evolution of the normalized translational (a) and vibrational (b) wall heat fluxes defined in equation (29).

agreement with the self-similar solution, are perfectly superposed until $Re_x \approx 6 \times 10^6$; afterwards, the LES predicts an earlier transition to turbulence and a wider transitional region. A similar behavior was already noticed for a perfect-gas turbulent boundary layer at Mach 2 in [25], which assessed the capability of the current numerical scheme in handling wall-resolved implicit LES. Even in this case, the breakdown to turbulence is slightly anticipated with respect to DNS, mainly due to the introduction of numerical and modeling errors. Sciacovelli *et al.* [25] pointed out that $\Delta z^+ < 10$ is an essential requirement to correctly capture the transition region dynamics, whereas the streamwise resolution was found to be less influential. The constraints are likely to be even stronger for the present case, given the much larger Mach and Reynolds numbers. Notwithstanding the differences in the transitional zone, the quality of the LES is high enough to provide a good estimation of the wall shear stress in the downstream fully-turbulent region. The evolution of the normalized wall heat fluxes $C_{q,w}^{\mathrm{TR}}$ and $C_{q,w}^{\mathrm{V}}$, defined as

$$C_{q,w}^{\mathrm{TR}} = \frac{\lambda_{\mathrm{TR}} \partial T / \partial y}{\rho_\infty u_\infty^3} \quad \text{and} \quad C_{q,w}^{\mathrm{V}} = \frac{\lambda_{\mathrm{V}} \partial T_V / \partial y}{\rho_\infty u_e^3} \tag{29}$$

are shown in figure 3. Similarly to the C_f distribution, the largest discrepancies between LES and DNS are found at the transition point. The $C_{q,w}^{\mathrm{TR}}$ contribution is also slightly underestimated in the fully turbulent region, which is mainly caused by a slightly smaller temperature gradient. The vibrational wall heat fluxes (which are one order of magnitude smaller than the translational counterparts) exhibit similar trends, with local peaks smeared out in the LES case and distributions in the fully-turbulent regions almost superposed.

We now focus on the comparison of wall-normal profiles in the turbulent portion of the domain. A preliminary analysis of the data has shown that the best agreement between DNS and LES is obtained when comparing streamwise stations having the same friction Reynolds number $Re_\tau = u_\tau \rho_w \delta_{99} / \mu_w$, rather than keeping the same Re based on the displacement of momentum thicknesses. As a consequence, wall-normal profiles are extracted at a fixed streamwise station having $Re_\tau = 1000$, corresponding to $Re_x = u_\infty \rho_\infty x / \mu_\infty = 14.43 \times 10^6$ for the DNS and 13.20×10^6 for the LES, respectively, Re_x being the Reynolds number based on the local distance from the leading edge. The profiles will be plotted against $y^+ = y/l_\nu$ with $l_\nu = \overline{\mu}_w/(\overline{\rho}_w u_\tau)$ and $u_\tau = \sqrt{\tau_w/\overline{\rho}_w}$, or in semi-local units $y^\star = \overline{\rho} u_\tau^\star y / \overline{\mu}$, with $u_\tau^\star = \sqrt{\tau_w/\overline{\rho}}$. We start from the classical scaling of Van-Driest [26] and Griffin-Fu-Moin [27] for the mean streamwise velocity in figure 4(a)-(b). The results show a fair agreement with the theoretical predictions of the logarithmic and linear laws for Van-Driest transformation; furthermore, an almost perfect collapse of LES profiles with the DNS data is observed, with only negligible differences in the wake region as previously pointed out by [5]. An underestimation of the logarithmic law is encountered in GFM transformation, previously observed in [10], for both DNS and LES. Similarly, comparisons of the mean density and translational temperature in figure 4(c)-(d) prove that the first-order mean thermodynamic quantities are correctly reproduced as well. On the contrary, some discrepancies start to appear on the distributions of the vibrational quantities. Indeed, the evolution
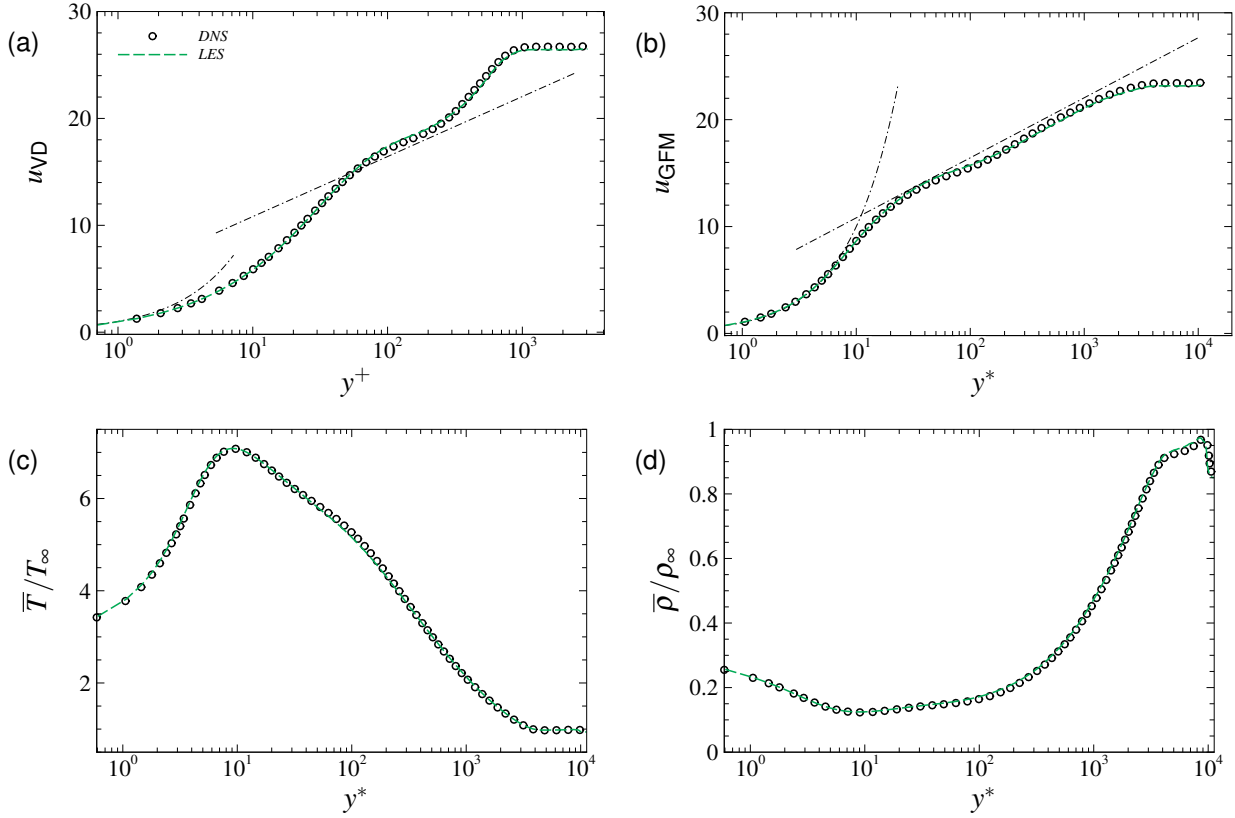
Figure 4 – Wall-normal evolution of mean quantities: Van-Driest transformed streamwise velocity (a),Griffin-Fu-Moin transformation (b), normalized mean temperature (c) and normalized mean density (d).

of the mean vibrational temperature, shown in figure 5(a), underestimates the local peak in the buffer region, whereas the correct behavior is recovered near the wall and in the outer part of the boundary layer. Such a behavior can be linked to errors in the estimation of the source terms in the vibrational energy equation. Since chemical activity is particularly weak (as already observed in [10]), the main source of vibrational energy variation is the translational-vibrational energy exchange, quantified by Q_{TV} in equation (5), which is computed according to Park's 2T as in equation (13). When the absolute value of this quantity goes to zero, the flow tends to a local thermal equilibrium state. This is what happens near the wall, due to the imposed isothermal conditions, and at the freestream, where $T = T_V = T_\infty$. Positive values of Q_{TV} denote a state of vibrational under-excitation, resulting in $\overline{T} > \overline{T_V}$. This happens in most of the boundary layer apart from a small region in the outer layer. The evolution of $\overline{Q_{TV}}$, shown in figure 5(b), reveals that the LES overestimates its value in the buffer region. This leads to an excess of internal energy transferred from the vibrational to the rototranslational modes, resulting in the reduction of T_V observed in figure 5(a). This inaccuracy is most likely caused by the simple approximation made in the LES computation for which

$$\overline{Q_{TV}} \approx \overline{Q_{TV}} \left(\widetilde{T}, \overline{p}, \widetilde{Y}_{n|n=1...NS} \right), \tag{30}$$

that is, the resolved translational-vibrational energy exchange is directly evaluated with the filtered aerothemochemical quantities. Therefore, neglecting the SGS turbulence-thermochemistry interactions introduces an important modeling error and further investigations are needed to develop a more suitable closure strategy. In a similar way, the chemical activity is altered due to incorrect source terms values. Figure 6(a) shows the mass fractions distributions of the predominant products in the mixture, that is, NO and O. Even in this case, modeling errors induce an underestimation of chemical dissociation, resulting in an amount of products mass fractions smaller of approximately 20%. This is a direct consequence of their smaller chemical production rates values, expressed in equation (12) and shown in figure 6(b), that justify the reduction of the total amounts of nitric oxide and atomic
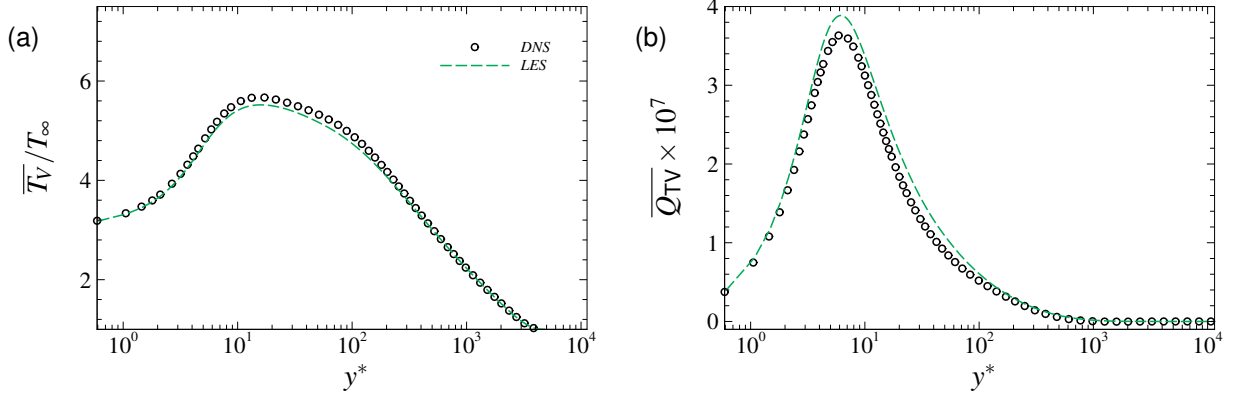
Figure 5 – Wall-normal evolution of normalized mean vibrational temperature (a) and translational-vibrational energy exchange source term (b).
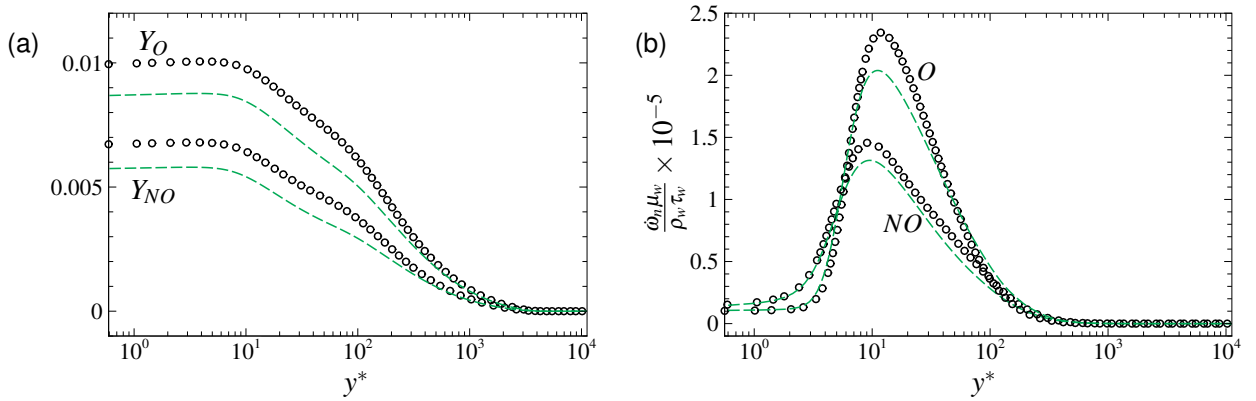

Figure 6 – Wall-normal evolution of major products mass fractions (a) and chemical source terms (b).

oxygen in the mixture. Nevertheless, given the small levels of chemical activity in the current configuration (as also witnessed by the order of magnitude of the products mass fractions) such errors have only a limited, almost negligible influence on the mean field. Particular attention must be paid, on the contrary, when larger temperature values come at play: if chemical activity is significantly triggered, an incorrect estimation of the mixture composition may lead to large errors in the evolutions of the mixture density and transport properties. These estimations may in turn influence the magnitude of diffusive fluxes in the governing equations, strongly altering the flow dynamics.

Despite the above mentioned approximations, second-order statistics are only mildly affected (see figure 7). The LES resolved Reynolds stresses are in fair agreement with the DNS reference throughout the boundary layer, apart from a slight reduction of the fluctuating streamwise velocity in correspondence of the peak of production, as previously observed in computations of supersonic boundary layers of calorically perfect gases [5]. Also the components of the vorticity fluctuations show a good collapse with the reference data. Thermodynamic fluctuating quantities, instead, are found to be overestimated with respect to the reference solution.

4. Conclusions

A hypersonic turbulent boundary layer at Mach ≈ 12, spatially developing over a cooled flat plate, is investigated by means of direct numerical simulations and large-eddy simulations to assess the capability of the under-resolved computation in capturing the dynamics of hypersonic turbulent flows at high enthalpies. The fluid is air, modeled as a five-species mixture by means of Park's 2T formulation. The free-stream thermodynamic conditions are such that thermochemical non-equilibrium is obtained inside the boundary layer, with vibrational relaxation effects being predominant with re-
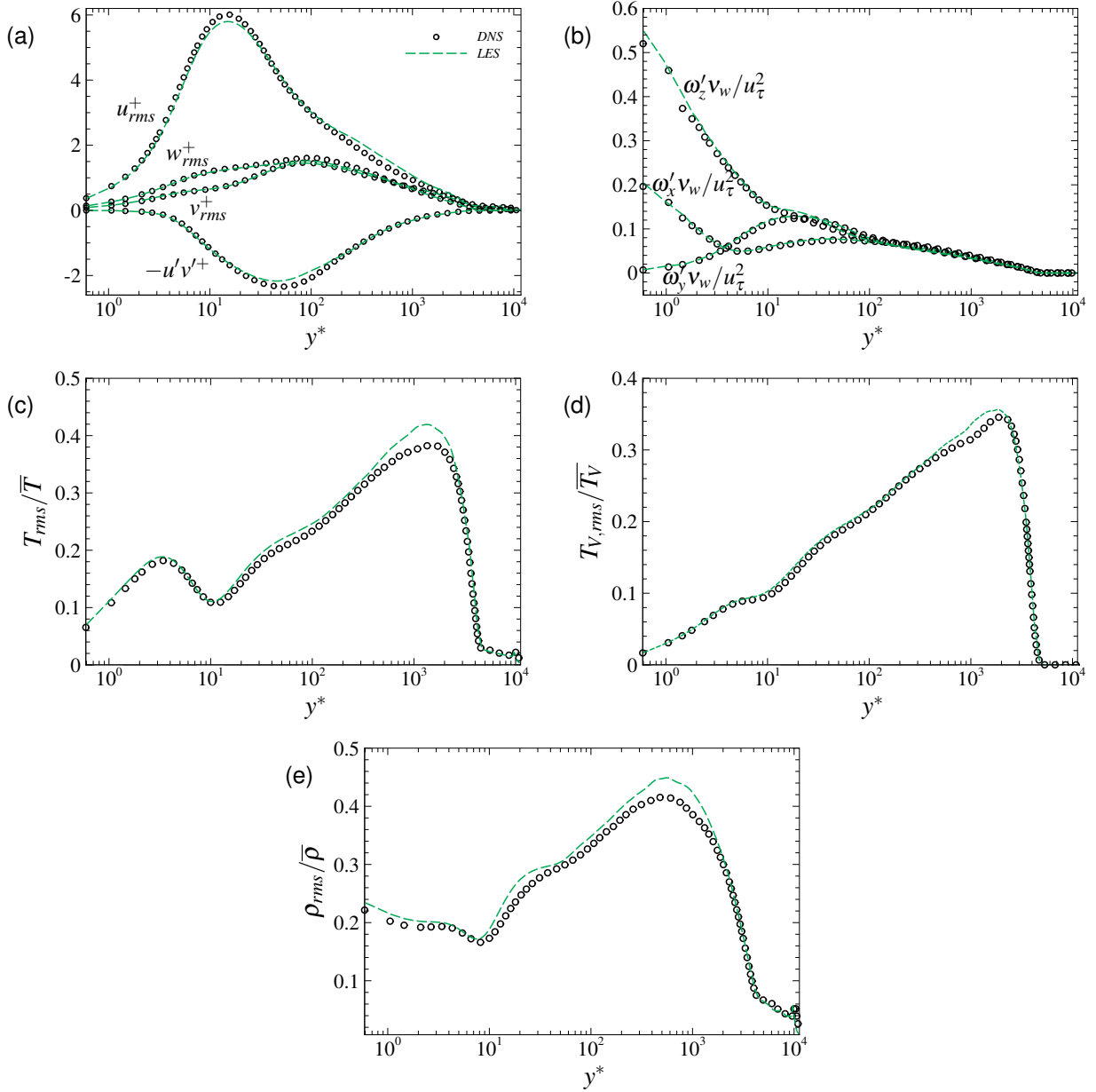
Figure 7 – Wall-normal evolution of fluctuating variables: velocity (a), vorticity (b), translational temperature (c), vibrational temperature (d) and density (e).

spect to chemical ones. Such a configuration was recently analysed from the physical standpoint by Passiatore *et al.* [10], who observed that vibrational non-equilibrium is sustained by the turbulent fluctuations, which efficiently redistribute the internal energy at larger rates than the vibrational relaxation ones. Given the high computational cost of performing such expensive simulations, the necessity of reducing the computational time is straightforward: in this work we assess the suitability of LES in a high-enthalpy configuration, systematically comparing the results with the reference DNS benchmark. It should be noted that the computational grid for the LES computation is such that Δy_w^+ is less than unity everywhere, avoiding the use of wall models which would add further modeling uncertainties and numerical errors.

The comparison has shown that the main first-order statistics present an acceptable agreement when compared at the same Re_τ. The largest discrepancies are shown in the transitional region, since large-eddy computations are known to anticipate the breakdown to turbulence. The evolution of fluctuating quantities has revealed that the Reynolds stresses are globally well reproduced, differently from the fluctuating values of temperatures and density that exhibit a clear discrepancy. Being one of the first LES in high-enthalpy conditions, no information are available in literature regarding the clo-

sure of chemical production rates and rate of energy exchange, since their formulations are strongly non-linear functions of mixture composition, temperature and pressure and require a fundamental investigation. As a result, this work is based on the assumption of evaluating the thermochemical source terms with the filtered quantities. The results showed that translational-vibrational energy exchange is overestimated by LES, resulting in a slightly smaller vibrational temperature and, overall, in a partly erroneous estimation of the distribution of internal energy among the energetic modes. The investigation of chemical activity showed instead an underestimation of dissociation chemical production rates and a consequent smaller amount of reaction products in the mixture composition. Nevertheless, the latter has not altered neither the mean density distribution nor the transport properties, since the temperatures at stake are not high enough to trigger a significant chemical activity. These important considerations have been pointed out in recent works [8, 9, 11, 10] by a priori considerations, and in this study they have been corroborated by quantifying the deficiencies and the consequences of such strong approximations.

The present numerical study is a first step towards the comprehension of the use of large-eddy simulations in the context of high-enthalpy flows. Given the excessive computational cost of DNS and the well-known inaccuracies of RANS simulations, large-eddy simulations represent an attractive compromise between accuracy and computational cost. By using LES, it would be possible to perform parametric studies spanning a reasonable range of control parameters, necessary to draw more general conclusions on the physics of high-enthalpy flows. However, the modeling of the new unclosed terms that arise when filtering the multi-component Navier–Stokes equations open new research questions. Further investigations are indeed needed to formulate suitable closures that incorporate the effect of SGS turbulence-thermochemistry interactions. Moreover, the effect of thermochemical source terms modeling strongly depends on the operating conditions, since thermal-relaxation phenomena would be predominant higher in the atmosphere or at higher densities, whereas a large kinetic energy content promote molecular collisions resulting in a more intense chemical activity. Investigating different thermodynamic conditions is of the utmost importance to understand how turbulence interacts with the thermochemical out-of-equilibrium field and the role of nonequilibrium phenomena in modulating the turbulent motions. These considerations are even more important for the successful use of wall models at high enthalpies, since the majority of the turbulence-thermochemistry interactions would happen in the strongly unresolved near-wall region. Testing different closures for the subgrid-scale activity is another important task that should be addressed, which represents the authors' ongoing work, together with the detailed exploitation of the present modeled SGS fluxes by a posteriori analyses.

5. Contact Author Email Address

Corresponding author Donatella Passiatore: donatella.passiatore@poliba.it

6. Copyright Statement

References

[1] Evangelos T Spyropoulos and Gregory A Blaisdell. Large-eddy simulation of a spatially evolving supersonic turbulent boundary-layer flow. *AIAA journal*, 36(11):1983–1990, 1998.

[2] H Yan, D Knight, and AA Zheltovodov. Large-eddy simulation of supersonic flat-plate boundary layers using the monotonically integrated large-eddy simulation (miles) technique. *J. Fluids Eng.*, 124(4):868–875, 2002.

[3] S Stolz and Nikolaus A Adams. Large-eddy simulation of high-reynolds-number supersonic boundary layers using the approximate deconvolution model and a rescaling and recycling technique. *Physics of fluids*, 15(8):2398–2412, 2003.

[4] A Hadjadj, O Ben-Nasr, MS Shadloo, and A Chaudhuri. Effect of wall temperature in supersonic turbulent boundary layers: A numerical study. *International Journal of Heat and Mass Transfer*, 81:426–438, 2015.

[5] O Ben-Nasr, A Hadjadj, A Chaudhuri, and MS Shadloo. Assessment of subgrid-scale modeling for large-eddy simulation of a spatially-evolving compressible turbulent boundary layer. *Computers & Fluids*, 151:144–158, 2017.

[6] X. I. A. Yang, J. Urzay, S. Bose, and P. Moin. Aerodynamic heating in wall-modeled large-eddy simulation of high-speed flows. *AIAA journal*, 56(2):731–742, 2018.

[7] L. Fu, M. Karp, S. T. Bose, P. Moin, and J. Urzay. Shock-induced heating and transition to turbulence in a hypersonic boundary layer. *Journal of Fluid Mechanics*, 909, 2021.

[8] M. Di Renzo and J. Urzay. Direct numerical simulation of a hypersonic transitional boundary layer at suborbital enthalpies. *Journal of Fluid Mechanics*, 912, 2021.

[9] D. Passiatore, L. Sciacovelli, P. Cinnella, and G. Pascazio. Finite-rate chemistry effects in turbulent hypersonic boundary layers: A direct numerical simulation study. *Physical Review Fluids*, 6(5):054604, 2021.

[10] Donatella Passiatore, Luca Sciacovelli, Paola Cinnella, and G Pascazio. Thermochemical non-equilibrium effects in turbulent hypersonic boundary layers. *Journal of Fluid Mechanics*, 941, 2022.

[11] J. Urzay and M. Di Renzo. Engineering aspects of hypersonic turbulent flows at suborbital enthalpies. *Annual Research Briefs, Center for Turbulence Research*, pages 7–32, 2021.

[12] F. Nicoud and F. Ducros. Subgrid-scale stress modelling based on the square of the velocity gradient tensor. *Flow, turbulence and Combustion*, 62(3):183–200, 1999.

[13] P. A. Gnoffo, R. N. Gupta, and J. L. Shinn. Conservation equations and physical models for hypersonic air flows in thermal and chemical nonequilibrium. Technical report, NASA Technical Paper 2867, 1989.

[14] C. Park. Two-temperature interpretation of dissociation rate data for N2 and O2. In *26th Aerspace Sciences Meeting*, page 458, 1988.

[15] C. Park. *Nonequilibrium Hypersonic Aerothermodynamics*. John Wiley and Sons, 1990.

[16] R. C. Millikan and D. R. White. Systematics of vibrational relaxation. *Journal of Chemical Physics*, 39:3209–3213, 1963.

[17] C. Park. Review of chemical-kinetic problems of future NASA missions. I-Earth entries. *Journal of Thermophysics and Heat transfer*, 7(3):385–398, 1993.

[18] F. G. Blottner, M. Johnson, and M. Ellis. Chemically reacting viscous flow program for multi-component gas mixtures. Technical report, Sandia Laboratory, 1971.

[19] J. O. Hirschfelder and C. F. Curtiss. *Molecular theory of gases and liquids*. John Wiley and Sons, 1969.

[20] CR Wilke. A viscosity equation for gas mixtures. *The Journal of Chemical Physics*, 18(4):517–519, 1950.

[21] T. Poinsot and D. Veynante. *Theoretical and numerical combustion*. R.T. Edwards, Inc., 2005.

[22] R. N. Gupta, J. M. Yos, R. A. Thompson, and K. P. Lee. A review of reaction rates and thermodynamic and transport properties for an 11-species air model for chemical and thermal nonequilibrium calculations to 30000 K. 1990.

[23] F. Ducros, V. Ferrand, F. Nicoud, C. Weber, D. Darracq, C. Gacherieu, and T. Poinsot. Large-eddy simulation of the shock/turbulence interaction. *Journal of Computational Physics*, 152(2):517–549, 1999.

[24] S. Gottlieb and C.-W. Shu. Total Variation Diminishing Runge-Kutta schemes. *Mathematics of Computation*, 67(221):73–85, 1998.

[25] L. Sciacovelli, D. Passiatore, P. Cinnella, and G. Pascazio. Assessment of a high-order shock-capturing central-difference scheme for hypersonic turbulent flow simulations. *Computers & Fluids*, 230(105134):1–23, 2021.

[26] E. R. Van Driest. *The problem of aerodynamic heating*. ARC, 1956.

[27] K. P. Griffin, L. Fu, and P. Moin. Velocity transformation for compressible wall-bounded turbulent flows with and without heat transfer. *Proceedings of the National Academy of Sciences*, 118(34), 2021.